RESEARCH ARTICLE

Mapping and Classification of the Liaohe Estuary Wetland Based on the Combination of Object-Oriented and Temporal Features

SIEN GUO[1,2], **ZIYI FENG**[1,2,3,4,5], **PENG WANG**[1,3], **JIE CHANG**[1,2], **HAO HAN**[1,2], **HAIFU LI**[5,6], **CHUNLING CHEN**[1,3,4], **AND WEN DU**[1,2,3,4,5]

[1]College of Information and Electrical Engineering, Shenyang Agricultural University, Shenyang 110866, China
[2]Liaoning Research and Application Center of Remote Sensing of Forest and Grass Resources and Environment (University-Enterprise Cooperation) for High-Resolution Earth Observation System, Shenyang 110866, China
[3]China National Digital Agriculture Regional Innovation Center (Northeast), Shenyang 110866, China
[4]Key Laboratory of Smart Agriculture Technology in Liaoning Province, Shenyang 110866, China
[5]Liaoning Panjin Wetland Ecosystem National Observation and Research Station, Shenyang 110866, China
[6]College of Water Conservancy, Shenyang Agricultural University, Shenyang 110866, China

Corresponding author: Wen Du (duwen@syau.edu.cn)

ABSTRACT For the protection, restoration, and sustainable management of wetland ecosystems, precision in extracting high-quality wetland land cover information is crucial. This study focused on the National Nature Reserve of Liaohe Estuary in Panjin City, Liaoning Province, China. To enhance the classification accuracy of wetland land covers exhibiting similar spectral characteristics and alleviate the occurrence of the 'salt-and-pepper' effect, where certain land parcels are erroneously classified into multiple categories by pixel-based methods, an approach integrating object-oriented techniques and temporal features was employed for precise wetland land cover classification. The analysis utilized multi-temporal Sentinel-2 multispectral images. Initially, the images underwent segmentation using the SNIC method to generate uniform polygons, effectively mitigating misclassification issues. Subsequently, texture, geometry, band reflectance, and spectral deviation features were extracted for each segmented object. A total of 57 features, including vegetation and moisture components, were integrated to construct temporal characteristics. By applying the Random Forest (RF) algorithm in combination with Extreme Randomized Trees (ERT), 18 significant features influencing wetland extraction were identified. These selected features were then utilized to train a Random Forest (RF) model for classifying wetland land cover in the study area. The findings revealed that the integrated object-oriented and temporal feature classification approach achieved an impressive overall accuracy of 95.52% and a Kappa coefficient of 0.95 for the Liaohe Estuary wetland region. The accuracy for various land cover types reached 0.87 for both user and producer accuracy. Compared to alternative machine learning algorithms such as SegUnet++, SVM, and RF, the proposed method demonstrated a performance increase of 16.35%, 14.06%, and 6.14%, respectively. The incorporation of temporal features notably reduced land cover misclassifications, resulting in a 6.14% increase in overall accuracy and a 0.07 improvement in the Kappa coefficient compared to a method lacking temporal features. Particularly for categories like canals, aquaculture, rivers, and reservoirs, producer accuracy improved by over 7.5% and user accuracy by more than 2.9%. The effectiveness of the object-oriented approach was evident in addressing the ''salt-and-pepper'' effect, showcasing a rise of 2.81% in overall accuracy and 0.03 in Kappa coefficient compared to an approach not utilizing object-oriented techniques. In summary, the proposed classification method, integrating object-oriented methods and temporal features, offers superior accuracy in fine wetland land cover classification and mapping.

The associate editor coordinating the review of this manuscript and approving it for publication was Dost Muhammad Khan.

INDEX TERMS Image classification, object-oriented methods, time series, tasseled cap transformation, random forest.

I. INTRODUCTION

Wetlands play a crucial role in maintaining essential ecological functions, including water source maintenance, water purification, flood control, drought resistance, climate regulation, and biodiversity conservation. Consequently, healthy wetland ecosystems are a critical component of the ecological security system and the foundation for sustainable economic and social development [1], [2], [3]. The Liaohe Estuary National Nature Reserve is situated in the Dawei District of Panjin City, Liaoning Province, and the Liaohe Estuary Ecological and Economic Zone. It is not only one of China's largest coastal estuarine wetlands but also one of the most comprehensive coastal wetland ecosystems worldwide [4]. This area not only harbors abundant biological resources but also serves as a breeding ground, wintering ground, and migratory bird stopover for various waterfowl species [5]. Unfortunately, in recent years, the Liaohe Estuary Wetland has encountered significant pressures from human activities and natural disturbances [6]. Hence, it is imperative to adopt appropriate management and monitoring methods to safeguard the wetland, accurately identify and measure the distribution of wetland features, and provide decision-making support for the conservation and management of the coastal wetland ecosystem in the Liaohe Estuary region.

In the realm of land cover classification, satellite remote sensing imagery offers advantages in terms of broad monitoring scope, promptness, and cost-effectiveness [7]. Some researchers have utilized the polarization properties of radar remote sensing data to enhance classification precision. While radar data are relatively resilient to cloud interference, they exhibit inherent boundary noise that poses challenges in suppressing, consequently diminishing the resolution of radiation. In contrast to radar remote sensing data, Sentinel-2 images boast high spatial resolution and quick revisit rates, showcasing promising capabilities in intricate wetland monitoring. Wang et al. undertook vegetation classification within the coastal wetlands of Yancheng using the random forest algorithm with Sentinel-2 imagery [8]. Ivanova et al. conducted the classification and mapping of the Straldzha Complex Protected Area utilizing Sentinel-2 satellite imagery [9]. Therefore, the present study employs Sentinel-2 images as the foundational data for classification purposes.

In recent years, a variety of machine-learning techniques have facilitated the swift and automated classification of wetlands. These methods encompass Support Vector Machine (SVM) [10], Random Forest (RF) [11], and K-Nearest Neighbor (KNN) [12], among others, and are often integrated with deep learning approaches such as FCN, SegNet, and U-Net for land cover extraction [13], [14]. Nevertheless, many of these methodologies primarily rely on pixel-based strategies, giving rise to the phenomenon known as the "salt and pepper effect," where identical land cover types are classified

into multiple disparate categories [15]. Object-Based Image Analysis (OBIA) offers a superior alternative by segmenting satellite imagery into homogeneous objects, thereby furnishing valuable shape, texture, and other features for wetland classification. For instance, Wang et al. applied the OBIA technique to Sentinel-1/2 temporal images, culminating in the production of a high-resolution (10-meter) map of East Asian wetlands [16]. In a similar vein, Zhang and Lin studied wetland classification in China's Dongting Lake region utilizing object-based and ensemble algorithms [17]. Studies indicate that object-based machine learning techniques exhibit exceptional efficiency and robustness in enhancing the accuracy and performance of wetland classification.

Wetland types pose a challenge due to their closely aligned spectral characteristics, making differentiation challenging compared to common land cover types. Within wetland types, aquaculture, rivers, canals, and reservoirs manifest similar spectral attributes and display spatial variation concerning watercolor, shape, and size, further complicating differentiation [18]. Scholars have incorporated various vegetation and water indices to establish time series aiding in wetland classification. For instance, Xu et al. integrated MODIS and Landsat normalized difference vegetation index (NDVI) time series for seasonal wetland classification at Poyang Lake [19]. Yan et al. utilized Landsat-8 NDVI and normalized difference water index (NDWI) time series data to construct a dataset for wetland classification [20]. Chen et al. leveraged MODIS data to develop an enhanced vegetation index (EVI) time series curve, incorporating the minimum distance method based on spectral matching for wetland classification in Dongting Lake [21]. Utilizing vegetation and water index time series as features has enhanced the overall classification accuracy to some extent. However, the use of pixel-based classification methods, along with the reliance solely on pixel-derived features, may be insufficient for accurately discriminating highly diverse wetlands. Variations in greenness can signal changes in vegetation and microbial growth, while shifts in wetness offer insights into lake hydrological characteristics and the dynamics of the entire wetland ecosystem [22]. Applying tasseled cap transformation to derive greenness and wetness as temporal features better captures seasonal changes in wetland land cover types, especially for evolving categories, yielding favorable results in extraction.

In light of the current status of the Liaohe Estuary wetland, a methodology that comprehensively considers the spatial characteristics and temporal dynamics of the wetland is essential for producing a distribution map of the area. This research employed 2022 Sentinel-2 data within the Google Earth Engine (GEE) platform and integrated time series attributes that capture the variations in vegetation greenness and moisture content in the wetland. By combining object-based analysis and temporal features, an inclusive approach

was developed. The findings of this study serve as a theoretical foundation for land cover delineation within the Liaohe Estuary wetland.

II. STUDY AREA AND DATA

A. STUDY AREA

The Liaohe Estuary National Nature Reserve is situated north of Liaodong Bay in Panjin City, Liaoning Province, China, spanning from 121°28′ E to 122°10′ E longitude and 40°32′ N to 41°3′ N latitude, showcasing remarkable coastal wetland resources and biodiversity conservation value. The coastal wetlands in the Liaohe Delta were designated as the Shuangtai Estuary National Nature Reserve in 1986 and were recognized as a Ramsar Wetland of International Importance in 2005 [23]. The reserve is situated in the northern temperate zone and features a semi-humid monsoon climate, with an average annual temperature of 8.4° and an average annual rainfall ranging from 611.6 to 640.0 millimeters [24], [25]. Fig. 1 depicts the location of the designated study area.
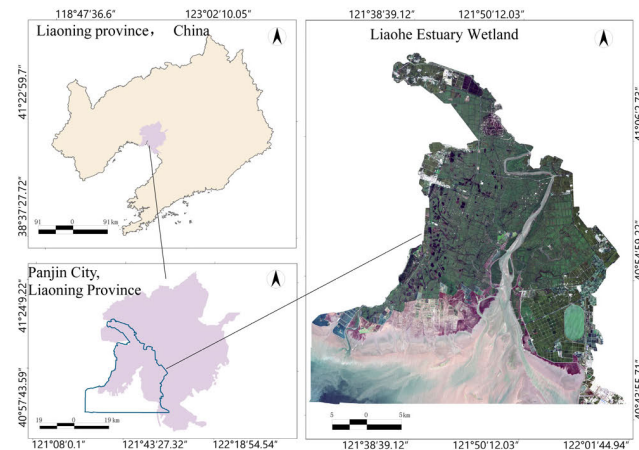

FIGURE 1. Schematic diagram of the study area.

B. DATA AND PREPROCESSING

1) SENTINEL-2 IMAGES AND PREPROCESSING

The data for this study comes from the Harmonized Sentinel-2 MSI: Multi-Spectral Instrument, Level-2A dataset on Google Earth Engine (GEE) [26]. This dataset represents the Earth's surface reflectance after atmospheric correction. Sentinel-2 is a wide-swath, high-resolution, multispectral imaging mission that supports land monitoring research, including vegetation, soil, and water cover monitoring, as well as observations in inland waterways and coastal areas. In this study, we first selected Sentinel-2 data from 2022 with a cloud coverage below 10% and created masks to remove clouds, cloud shadows, and cirrus clouds from the image data. Finally, we selected images that had over 95% cloud-free pixel coverage within the study area and filled in missing values using monthly composite imagery. The available dates of the images are listed in the Table below. This study primarily focuses on land cover type extraction from the image on September 8, 2022.

TABLE 1. SENTINEL-2A Imagery.

Date	Orbit Number/ Cloud Cover (%)	
	51TUF	51TVF
2022-01-26	8.664563	7.580077
2022-02-05	1.905764	7.674418
2022-02-25	2.650472	2.848329
2022-03-02	1.596624	4.858881
2022-03-07	0.839032	3.455118
2022-04-01	8.148445	6.440452
2022-04-16	3.835236	6.17513
2022-04-26	7.739039	7.988849
2022-09-08	0.005362	0.003656
2022-09-18	0.009894	0.010805
2022-10-18	0.260323	0.100682
2022-10-28	1.054661	3.960451
2022-12-07	2.124127	2.333458

2) SAMPLE DATA

Based on the land use classification system of the remote sensing monitoring database and the Wetland Classification (GB/T 24708-2009) in China, and in consideration of the land use situation in the study area, this research developed a land cover classification scheme for the Liaohe Estuary National Nature Reserve.
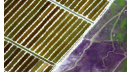
The land cover in the area was classified into 12 categories: river, building, road, restoration area, paddy field, reservoir, aquaculture, tidal fat, Suaeda salsa, oil well, canal, ditch, and reed. The specific interpretation signs can be found in Table 2. The study was based on the establishment of sampling sites at the Liaoning Panjin Wetland Ecosystem National Observation and Research Station, Shenyang, China. In September 2022, on-site field sampling was carried out for ten land cover categories, which included reeds, Suaeda salsa, oil wells, roads, Restoration area, canals, tidal flats, buildings, aquaculture, and paddy fields. Ten sampling locations were designated for each category. A sample dataset consisting of 2400 points was established by integrating Sentinel-2 images, Google Earth maps, and on-site field sampling, with 200 points allocated to each category. The training and testing datasets were split in a random 6:4 ratio. For the distribution of the sample points, please refer to Fig. 2.

III. RESEARCH METHODS

This study introduces a wetland classification method that combines object-oriented features and temporal features, aiming to improve the accuracy of wetland classification and reduce the "salt-and-pepper effect" in the results. Fig. 3 displays the technical roadmap of the study.

The study mainly focuses on processing the time-series data from Sentinel-2 and performing object-oriented image segmentation. The research investigates object-oriented classification methods for the wetland area in the Liaohe Estuary, aiming to achieve more precise land cover classification through feature extraction, feature selection, and comparative experiments. During the data preprocessing stage, the time-series images are processed to remove clouds and synthesize daily images, selecting those that cover over 95% of

TABLE 2. Classification and symbolic representation of wetland categories.

Primary Classification	Secondary Classification	Sentinel-2A imagery	Primary Classification	Secondary Classification	Sentinel-2A imagery
Natural Wetland	River			Reservoir	
	Reed			Aquaculture	
	Suaeda salsa		Artificial Wetland	Paddy fields	
	Tidal flat				
Non-wetland	Roads			Canal, ditch	
	Oil well				
	Building			Restoration area	

FIGURE 2. Distribution of samples in the training and validation datasets.

the study area. Afterward, the monthly synthesized images are used to fill gaps caused by cloud cover and generate a 2022 image sequence for analysis. Object-oriented segmentation is applied to segment the images and obtain a collection of diverse objects. Additionally, 12 land cover categories are visually interpreted to obtain sample points, which are then randomly divided into training and test sets. These segmented object collections, along with the sample points from the training set, form the data foundation for subsequent feature extraction. Feature extraction is performed on the segmented object collections obtained during the data preprocessing stage. These features comprise multi-temporal

temporal features, single-temporal spectral features, single-temporal standard deviation features, single-temporal texture features, and single-temporal geometric features. These five types of features comprehensively describe the characteristics of land cover in the wetland area of the Liaohe Estuary wetland, providing strong support for subsequent classification. Subsequent steps involve feature selection and separability verification, yielding a feature set closely linked to the land cover in the wetland area of the Liaohe Estuary. This selected feature set is labeled as the ''optimal'' feature set and employed for supervised classification training. Finally, in the comparative experiment stage, we combine all the extracted features, including the selected ''optimal'' features, and design four sets of experiments to analyze the impact of object-oriented classification, multi-temporal temporal features, and feature selection on the classification results. This process verifies the advantages and feasibility of the research methodology employed.

A. SEGMENTATION OBJECTS GENERATION USING SNIC

SNIC (Simple Non-iterative Clustering) is an object-oriented image segmentation method that integrates super-pixel technology with the principle of normalized cuts, it has been widely applied in object-oriented land cover classification [27], [28]. It aims to partition the image into compact regions with spatial continuity, thereby reducing redundant information. SNIC utilizes a regular grid to generate K seed pixels on the image plane, initializing centroids $C[k] = \{x_k, c_k\}$ This process generates k corresponding elements $e_i = \{x_i, c_i, k, d_{i,k}\}$, here, x_i denotes the spatial position of
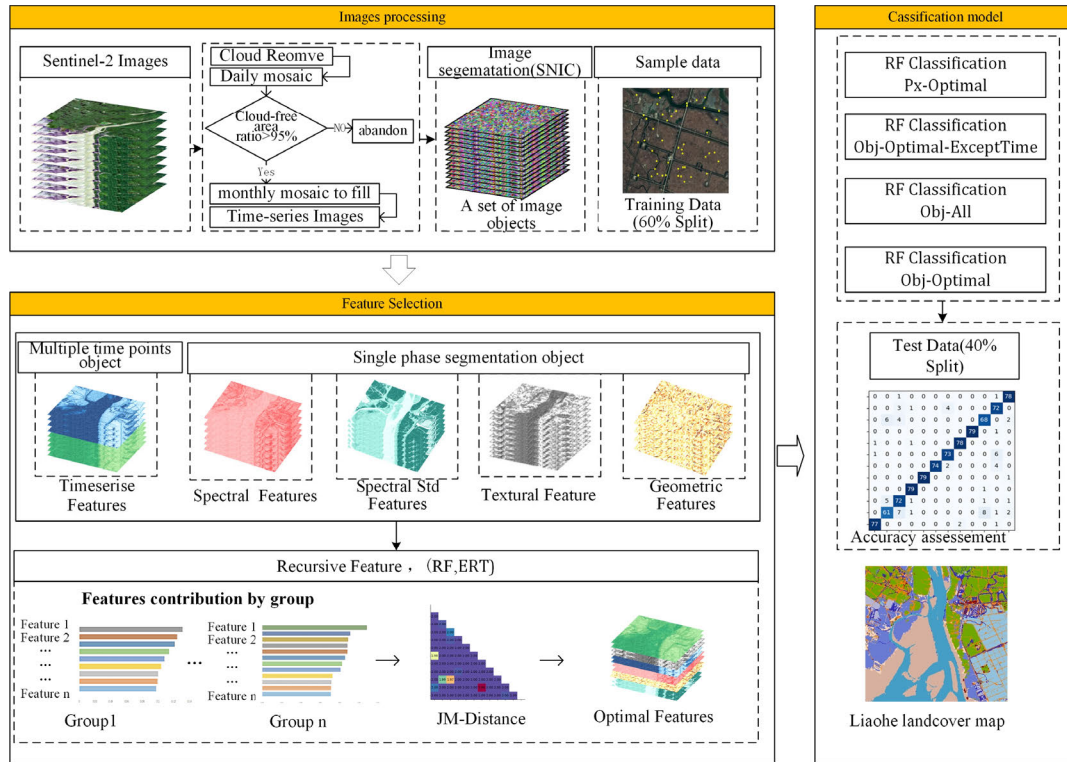
FIGURE 3. Overview of the experimental workflow.

the i-th element, c_i represents the L* a*b* color developed by the International Commission on Illumination(CIELAB) color, k represents the unique label of the superpixel (ranging from 1 to k), and $d_{i,k}$ signifies the distance from the i-th pixel to the centroid of the k-th superpixel, computed as shown in formula 1.

$$d_{i,k} = \sqrt{\frac{x_i + x_{k2}^2}{s} + \frac{c_i + c_{k2}^2}{m}} \qquad (1)$$

The variables s and m denote the normalization factors for spatial distance and color distance, respectively. m is recognized as the compactness factor. A greater value of m tends to generate square-like super-pixels; however, it may compromise boundary adherence. When m is assigned a value of zero, the spatial distance weighting feature is deactivated.

1. The k initial elements $d_{i,k}$ are all initialized to 0, and a priority queue Q is created with these elements. While Q is not empty, the element with the smallest distance is dequeued. The indicated pixels are consolidated into the k-th superpixel, and their values are set to the average of all pixels in the k-th superpixel, which is dynamically updated as new pixels are added.

2. For each neighboring pixel (in 4 or 8 directions) of the dequeued element, if the pixel has not yet been included in a superpixel, a new element e_i is generated and enqueued.

3. During the iteration of the algorithm, the dequeued elements are consolidated into their respective superpixels, and neighboring new elements that have not been included in a superpixel are enqueued.

4. The SNIC algorithm terminates when all pixels have been aggregated and Q is empty.

The final segmentation result consists of regions that exhibit both color and spatial similarity while preserving spatial continuity. This study employed the SNIC image segmentation algorithm within the Google Earth Engine (GEE) to segment the imagery captured on September 8, 2022. Due to the enhanced distinguishability of different land features in the available images for September, experimentation was conducted using the imagery from September 8th.

Seeds affect the distribution of distance for the segmentation objects. Excessive values will lead to distant seed distribution, resulting in large and coarse segmentation units. Insufficient values will result in closeness, causing overly fragmented segmentation. Setting seeds to 1 indicates pixel-based segmentation. Furthermore, connectivity can be set to either 4 or 8, determining whether homogeneity evaluation occurs in 4 or 8 directions. Both parameters influence the outcomes of the segmentation. After several trials, we finalized the segmentation parameters as 10 for seeds and 4 for connectivity. The SNIC image segmentation algorithm in GEE was employed in this study to generate compact and nearly uniform polygons.

B. FEATURES FROM SEGMENTATION OBJECTS

This study extracted a total of 57 features for all image objects. These features were categorized into five groups: single-temporal spectral features (9), spectral standard deviation (9), texture (13), geometric (4), and multi-temporal

TABLE 3. Feature categories and features.

Feature Categories		Features
Single-temporal features.	Spectral Features	Mean Blue (Blue), Mean Red (Red), Mean Green (Green), Mean NIR(NIR), Mean Red Edge 2(RE2), Mean MIR1(MIR1), Mean MIR2(MIR2), MeanWetness (Wetness), Mean Greenness (Greenness)
	Spectral Standard Deviation Features	Standard Deviation Blue (StdBlue), Standard Deviation Green (StdGreen), Standard Deviation Red (StdRed), Standard Deviation NIR (StdNIR), Standard Deviation Red Edge 2 (StdRE2), Standard Deviation MIR1(StdMIR1), Standard Deviation MIR2(StdMIR2), Standard Deviation Wetness (StdWetness), Standard Deviation Greenness (StdGreenness)
	Textural features	Angular Second Moment (ASM), Contrast (CONTRAST), Correlation (CORR), Variance (VAR), Inverse Difference Moment (IDM), Sum Average (SAVG), Sum Variance (SVAR), Sum Entropy (SENT), Difference variance (DVAR), Difference entropy (DENT), Entropy (ENT), Information Measure of Corr. 1(IMCORR1); Information Measure of Corr. 2(IMCORR2)
	Geometric features	Perimeter, Area, Width, Height
Multi-temporal temporal features.	Timeserise Features	TCG0126, TCW0126, TCG0205, TCW0205, TCG0225, TCW0225, TCG0302, TCW0302, TCG0307, TCW0307, TCG0401, TCW0401, TCG0416, TCW0416, TCG0426, TCW0426, TCG1018, TCW1018, TCG1028, TCW1028, TCG1207, TCW1207

time series features (22). These five feature sets are designed to encapsulate the spectral characteristics, wetness, greenness, texture, geometric shape, and temporal variations of land features. They provide a depiction of the distinct characteristics exhibited by various land types from diverse angles. Beyond the singular temporal feature descriptions, we employ a method that integrates multiple temporal phases. This approach not only intricately unveils the land features on the observed date but also assimilates variations in greenness and wetness from other temporal points throughout the entire year into the feature dimensions, introducing a crucial temporal consideration. This holistic representation enables us not only to capture the instantaneous state of land features on a given day but also to integrate the temporal dimension into feature engineering, highlighting the temporal evolution of land features as a vital aspect of our analysis. Refer to Table 3 for the complete list of features and their respective categories.

1. Single-temporal spectral features: Spectral features encompass the original reflectance values of the spectrum, as well as indices derived from the underlying spectral data. These features can depict the extent of spectral reflection by various objects and emphasize the spectral properties of the land surface. The greenness component in the Tasseled Cap Transformation is associated with vegetation coverage, leaf area index, and biomass. The wetness component indicates the soil moisture condition. Previous studies have demonstrated the advantages of both the wetness component and the greenness component in Tasseled Cap Transformation for wetland land cover classification [29], [30]. The calculation formulas are provided in (2) and (3).

$$\text{Wetness} = 0.0649 \times \text{b1} + 0.1363 \times \text{b2} + 0.2802 \times \text{b3} + 0.3072 \\ \times \text{b4} + 0.5288 \times \text{b5} + 0.1379 \times \text{b6} \\ - 0.0001 \times \text{b7} - 0.0807 \times \text{b8} - 0.0302 \times \text{b9} - 0.4064 \\ \times \text{b11} - 0.5602 \times \text{b12} - 0.1389 \times \text{b8A} \quad (2)$$

$$\text{Greeness} = -0.0635 \times \text{b1} - 0.1128 \times \text{b2} - 0.1680 \times \text{b3} \\ - 0.3480 \times \text{b4} - 0.3303 \times \text{b5} + 0.0852 \times \text{b6} \\ + 0.3302 \times \text{b7} + 0.3165 \times \text{b8} + 0.0467 \times \text{b9} \\ - 0.4578 \times \text{b11} - 0.4064 \times \text{b12} + 0.3625 \\ \times \text{b8A} \quad (3)$$

In the equation, b1, -b9, b11-b12, and b8A correspond to the bands 1 to 9, 11, 12, and 8A of Sentinel-2. In this study, spectral features and the moisture index-greenness index are computed by utilizing multiple spectral band layers from the image on September 8, 2022. In the object-oriented approach, the study determines the average value within individual segmented objects.

2. Single-temporal standard deviation features: Standard deviation is a statistical measure utilized to quantify the variation or distribution of pixel values within an image. It measures the differences between the individual pixel values within a segmented object and the mean value of the image, illustrating the extent of brightness or color variation present. Standard deviation finds various applications in image processing, encompassing image quality assessment, noise detection, and edge detection. The standard deviation of an image can be obtained by calculating the differences between each pixel and the mean, squaring these differences, summing them, averaging the sum, and then taking the square root. A larger standard deviation signifies greater variations in pixel values within the segmented object, while a smaller standard deviation indicates minor variations. It assists in analyzing the degree of change and statistical characteristics of the image. The formula for calculating standard deviation is given below:

$$\sigma = \sqrt{\left[\sum (x - \mu)^2 / N \right]} \quad (4)$$

In (4), symbols are used to represent statistical measures. σ represents the standard deviation, Σ signifies the summation operation which involves summing all the pixels in the image, x denotes the value of each pixel, μ represents the mean, which is the average value of all the pixel values, and N represents the total number of pixels in the image. In the object-oriented method, we calculate the standard deviation index for each segmented object derived from the September 8 segmentation outlined in Section III, part A. In the pixel-based method, the standard deviation features are calculated, covering the entire image.

3. Single-temporal texture features: Texture measures have been widely employed in the classification of land cover in remote sensing data, both in pixel-based and object-based approaches [31], [32], [33], [34]. The Gray-Level

Co-occurrence Matrix (GLCM) is the commonly used technique to extract local texture information from remote sensing images. The GLCM method involves traversing the image, counting the occurrences of pixel pairs with different gray levels, constructing a 2D matrix, and subsequently normalizing it. Subsequently, texture features can be extracted from the GLCM [35], [36], [37]. A total of 18 texture features can be generated using the GLCM approach.

In this study, feature selection entails the selection of 13 statistical measures from a total of 18 texture features. Within the pixel-based approach, green, near-infrared and red bands of Sentinel-2 imagery acquired on September 8th are selected. A gray-scale image called "Gray" is generated as the input for GLCM by employing a weighted linear combination (5) [38]. The input image for GLCM in the object-based approach is the cluster layer obtained through SNIC segmentation. Both the pixel-based and object-based approaches utilize GLCM with a sliding window of size 3 to extract the set of 13 statistical measures.

$$Gray = 0.3NIR + 0.59Red + 0.11Green \quad (5)$$

In (5), NIR represents the reflectance in the near-infrared band, RED represents the reflectance in the red band, and Green represents the reflectance in the green band.

4. Single-temporal geometric features: Geometric features refer to quantitative or qualitative descriptions of the properties and characteristics of shapes following segmentation. This study focused on selecting geometric information on the shape and size of image objects observed on September 8th. In this analysis, four fundamental geometric features were employed, encompassing measurements of the object's extent, including length, width, area (indicating the number of pixels within the image object), as well as perimeter [39], [40].

5. Multi-temporal temporal features: Temporal features at various time points are utilized to depict the spatiotemporal evolution of wetness and greenness components of segmented objects throughout the year. The calculation equations can be found in formulas 2 and 3. Based on experimentation, time series features acquired on September 18th exhibit a notable influence on the overall feature selection. Presumably, owing to the strong correlation between September 18th and September 8th, the wetness and greenness indices of the available images throughout the year are chosen as temporal features, amounting to a total of 22 bands, while excluding September.

C. FEATURE SELECTION BASED ON THE INTEGRATION ALGORITHM OF RANDOM FOREST AND EXTREME RANDOMIZED TREES

Random Forest (RF) is a method used to calculate the importance of features based on their frequency in the random forest and their contribution to node splitting. The feature importance scores are accumulated for each decision tree. Finally, the random forest calculates the average of the scores from multiple trees to obtain the standardized importance scores for each feature. Features with higher scores have greater importance for the overall performance of the model.

Extreme Randomized Trees (ERT) is an ensemble learning technique that analyzes the extent to which impurity is reduced for each feature during the construction of multiple decision trees. The algorithm tracks the number of times each feature is used for splitting and the level of impurity reduction caused by each split. These scores are typically averaged or summarized across multiple trees and subsequently normalized [41], [42].

Both models are capable of assessing feature importance, with the algorithms taking into account the complex interplay among multiple features, effectively mitigating overfitting and showcasing robust generalization. When the two models are merged and the feature importance values from both algorithms are averaged, a more dependable and comprehensive estimation of feature importance can be achieved, leading to enhanced guidance in feature selection [43], [44].

Based on these two algorithms, the feature selection process in this study is as follows:

1. Before conducting feature evaluation, we first group the features. To improve the stability and accuracy of the results, and to consider different aspects of the data comprehensively.

2. For each group, we separately compute the feature importance using the RF and ERT methods ten times and subsequently average the results to evaluate the importance of each feature for each group and category.

3. Sort the feature importance within each group.

4. Select features with high importance.

5. Calculate the JM distance for the selected feature set in the 12-class category to assess the separability of the features.

D. WETLAND LAND COVER CLASSIFYING WITH RANDOM FOREST METHOD

Classification and regression tree (CART), random forest (RF), and support vector machine (SVM) are machine learning techniques commonly used for land use and land cover (LULC) classification in remote sensing imagery [45], [46]. RF generally outperforms other popular classifiers and has proven superiority in various scenarios, particularly in the classification of complex wetlands [47], [48], [49]. RF is an ensemble learning algorithm that consists of multiple independent decision trees. During the training process, features are randomly selected for splitting, and bootstrap sampling is used to obtain different subsets of training data. The predictions of each tree are then combined through majority voting or averaging [50], [51].

One important parameter in RF is the number of trees. We explore this parameter from 20 to 1000 with a step size of 10 to determine the optimal value.

In this study, the feature set obtained in Section III, part C is input into the RF classifier for accuracy evaluation. The impacts of object-based methods, temporal features, and the selected features on land cover extraction accuracy are investigated in this study. Four experiments are conducted for comparative analysis.

The first group performs pixel-based classification using the optimized feature set identified through Random Forest and Extreme Randomized Trees on the training set. This group is labeled as "Px-Optimal" and aims to compare the differences between object-based and pixel-based methods in wetland extraction.

The second group uses the object-based method and applies the optimized feature set excluding temporal features. It is labeled as "Obj-Optimal-ExceptTime" and aims to evaluate the importance of temporal features in the selected features.

The third group uses the object-based method and incorporates all features. The classification performance is evaluated without any feature set optimization. It is labeled as "Obj-All" and aims to assess the effectiveness of feature selection.

The fourth group uses the object-based method and applies the optimized feature set. It is labeled as "Obj-Optimal" and aims to evaluate the importance of the selected features.

E. METHODS FOR ACCURACY ANALYSIS AND FEATURE SEPARABILITY EVALUATION

The confusion matrix is the standard approach to evaluating classification accuracy by comparing the classification outputs with ground truth data [52]. For accuracy evaluation, all samples from the test set, as described in Section II, part B were utilized. The evaluation methods include overall accuracy (OA), kappa coefficient, producer's accuracy (PA), and user's accuracy (UA) [53]. The specifics (6)-(9) are provided below:

$$OA\ (\%) = \frac{\sum_{i=1}^{n} p_{ii}}{N} \times 100 \quad (6)$$

$$Kappa = \frac{N \sum_{i=1}^{n} P_{ii} - \sum_{i=1}^{n} (P_{i+} \times P_{+i})}{N^2 - \sum_{i=1}^{n} (P_{i+} \times P_{+i})} \quad (7)$$

$$UA\ (\%) = \frac{P_{ii}}{P_{+i}} \times 100 \quad (8)$$

$$PA\ (\%) = \frac{P_{ii}}{P_{i+}} \times 100 \quad (9)$$

Within the given formula, n denotes the total number of columns within the confusion matrix, which corresponds to the total number of categories. P_{ii} indicates the count of accurately classified samples in both the i-th row and i-th column of the confusion matrix. P_{i+} denotes the total numbers of samples in the row i, while P_{+i} represents the total numbers of samples in the column i. N represents the total count of samples utilized for validation purposes.

Jeffries-Matusita (JM) distance is extensively employed in the field of pattern recognition and feature selection to evaluate category separability based on the assumption of a normal distribution of data [54]. This study assesses the separability of the selected features created in Section III, part C by calculating the JM distance. Statistical analysis was performed using all training samples from each land cover category.

The separability criterion (JM) between the two target land cover classes w_i and w_j can be defined as follows, using the training sample set C $(i, j = 1, 2, \ldots, C, i \neq j)$.

$$J_{ij} = 2 \left(1 - e^{-d_{ij}} \right) \quad (10)$$

Within the (10), d_{ij} denotes the Bhattacharyya distance between the two target land cover classes w_i and w_j.

$$d_{ij} = -\text{In} \left(\int \sqrt{P\ (x/w_i)\ P\ (x/w_j)} dx \right) \quad (11)$$

Within the (11), $P\ (x/w_i)$ and $P\ (x/w_j)$ denote the conditional probability density functions of the random variable x for the land cover classes w_i and w_j, respectively. It is generally assumed that these functions follow a multivariate normal distribution.

$$d_{ij} = \frac{1}{8} (m_j - m_i)^{\text{T}} \left(\frac{\Sigma_i + \Sigma_j}{2} \right)^{-1} (m_j - m_i)$$
$$+ \frac{1}{2} \text{In} \left(\left| \frac{\Sigma_i + \Sigma_j}{2} \right| \Big/ \sqrt{|\Sigma_i| |\Sigma_j|} \right) \quad (12)$$

Within the (12), m_i and m_j denote the means, while Σ_i and Σ_j represent the covariance matrices of w_i and w_j, respectively. The superscriptT indicates the transpose of the matrix.

IV. RESULTS

A. RESULTS OF FEATURE SELECTION AND SEPARABILITY

To enhance the model's time performance and facilitate its application in a wider research area, we categorized the 57 features mentioned in Table 3 (Section III, part B) into 5 groups for feature selection. From these, we selected a total of 18 features, and the results of this selection process for each group are depicted in Fig. 4.

Fig. 4. displays the ranking of feature importance scores, ranging from 0 to 1, representing the significance of each feature within its respective group. In Fig. 4(a), we performed multiple experiments on the temporal feature group, setting a significance threshold of 0.045. This ensured the retention of the top 50% of temporal features based on their importance rankings. The selected features include TCW0401, TCW0426, TCG1018, TCG0426, TCG1207, TCW1207, TCG0401, TCW1018, TCW1028, TCG0225, and TCW0416, totaling 11 features. Fig. 4(b) reveals that we chose the top 3 features (Wetness, NIR, and MIR1) for the spectral feature group. In Fig. 4(c), we selected the first feature (StdMIR1) for the std feature group. Within the texture feature group, we focused on the information measure of the first feature, IMCORR2, as indicated in Fig. 4(d). Lastly, in the spatial feature group, we prioritized the top 2 features, Perimeter and Area, as shown in Fig. 4(e).

Based on the results of feature selection, we evaluated the ability to distinguish between the 12 classes (Table 2). This involved assessing whether the selected features could effectively discriminate among the 12 land covers. Following the formula (8) in Section III, part E, we calculated the JM distance for the 18 selected features, and the results are presented in Fig. 5. The JM distances for all the feature pairs exceeded 1.9, with a maximum value of 2 and a minimum
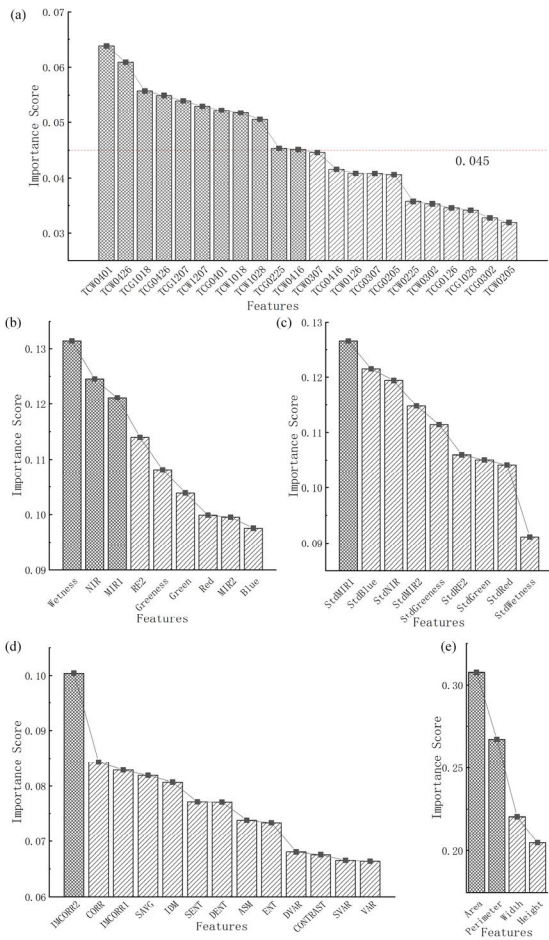
FIGURE 4. Feature selection results: (a) result of temporal feature selection, (b) result of original band selection, (c) result of std feature selection, (d) result of texture feature selection, (e) result of shape geometric feature selection.

FIGURE 5. The JM distance of 12 land cover categories under 18 selected features after feature selection.

FIGURE 6. Selection results of four experimental parameters: (a) parameter selection result for Experiment 1, (b) parameter selection result for Experiment 2, (c) parameter selection result for Experiment 3, (d) parameter selection result for Experiment 4.

value of 1.96, indicating a strong separability among the features for the 12 land covers. Therefore, research requirements have been met [55].

B. OPTIMAL PARAMETER SELECTION RESULTS

To conduct a more accurate comparison of the performance of the four experiments in Section III, part D, a parameter optimization experiment was designed specifically for the number of decision trees in the random forest (RF). The parameter selection experiment began with an initial value of 20 decision trees, which was incrementally increased by 10 until reaching 1000. The parameter optimization result was determined based on the value that achieved the highest overall classification accuracy while having the smallest parameter value. The experimental results are presented in Fig. 6. Fig. 6 graphically illustrates the relationship between overall accuracy and the parameter, where the blue line depicts the change in overall accuracy, the orange line represents the Kappa coefficient, the red dot indicates the position of the highest overall accuracy encountered during the parameter traversal, and the green dot represents the point of highest
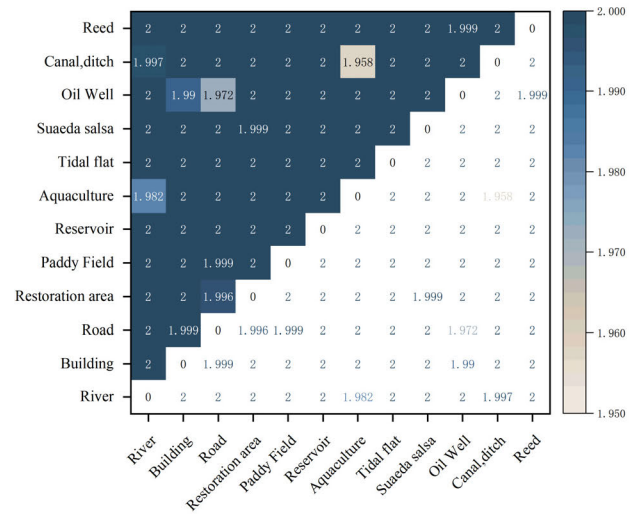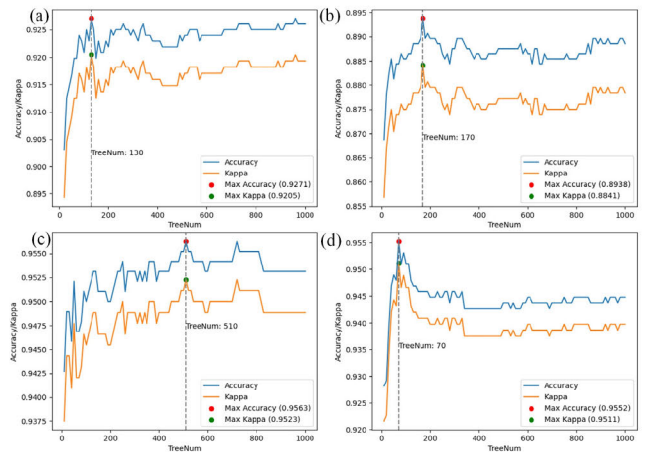
Kappa coefficient encountered during the traversal process. Fig. 6(a) displays the results of Experiment 1 (designated as Px-Optimal), and it is evident from the figure that the parameter value of 130 corresponds to the highest achieved accuracy. Fig. 6(b) presents the results of Experiment 2 (referred to as Obj-Optimal-ExceptTime), demonstrating that the parameter value of 170 yields the highest overall accuracy. The results of Experiment 3 (designated as Obj-All) incorporating temporal features are depicted in Fig. 6(c), where the parameter value of 510 yields the highest overall accuracy. Fig. 6(d) illustrates the results of Experiment 4 (referred to as Obj-Optimal), where the parameter value of 70 corresponds to the highest achieved overall accuracy and Kappa coefficient. In conclusion, the number of decision trees for the four experiments was set as follows: 130, 170, 510, and 70. These parameters will be used for comparing the optimal accuracy in subsequent analyses.

C. EVALUATION OF CLASSIFICATION ACCURACY

1) RESULTS OF VISUAL INTERPRETATION FOR ACCURACY

Based on the four experimental designs presented in Section III, part D the study area was classified using the optimal number of decision trees (see Section IV, part B). The classification results for the four experiments are depicted in Fig. 7.
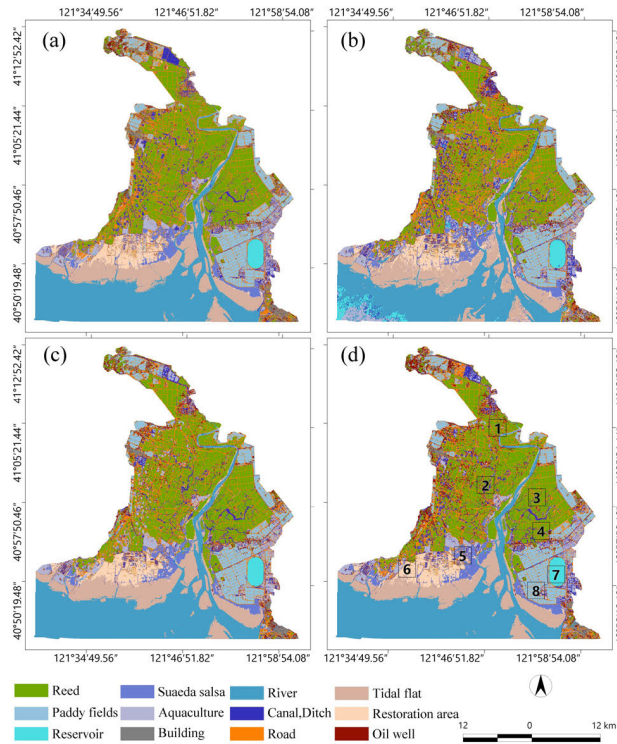

FIGURE 7. A comparative analysis of experimental results. (a) Px-Optimal experiment results, (b) Obj-Optimal-ExceptTime experiment results, (c) Obj-All experiment results, and (d) Obj-Optimal experiment results.

From the perspective of utilizing object-oriented technology were utilized, experiments 2-4 in Figs. 7(b-d) all employed object-oriented classification methods and exhibited clearer outlines. Among them, experiment 4 (Obj-Optimal) in Fig. 7(d) demonstrated a higher degree of compactness based on the object-oriented approach for both Suaeda salsa and reed land cover classes. For the classes of reservoir, canal, ditch, and oil well land cover the geometric shape of the boundaries was clearer, maintaining a high degree of consistency between the classes and shapes. This is mainly due to object-oriented technology is based on meaningful objects, rather than individual pixels. Additionally, Experiments 2-4 in Figs. 7(b-d) exhibited fewer salt and pepper noises compared to Experiment 1 (Px-Optimal) in Fig. 7, particularly for the Suaeda salsa, reed, and road classes. This indicates that the object-oriented approach has advantages in wetland extraction, mitigating the occurrence of the "salt and pepper" phenomenon prevalent in pixel-based methods.

Regarding the presence of temporal features, Experiments 1, 3, and 4 as depicted in Figs. 7(a, c, and d) all employed temporal features for classification, while Experiment 2 in Fig. 7(b) suffered from significant misclassification. As displayed in Fig. 7(b), Experiment 2 exhibited significant misclassifications wherein the river was incorrectly classified as tidal flats, reservoir, canal, ditch, or aquaculture; the reservoir was predominantly misclassified as a canal, ditch and the Suaeda salsa was misclassified as restoration area or tidal flats. This is mainly due to the high correlation between the land cover classes of canal, ditch, Suaeda salsa, and tidal flats. Therefore, incorporating temporal features improves the accuracy of wetland land cover classification. In conclusion, both object-oriented and temporal features can mitigate issues related to boundary clarity, salt and pepper noises, and misclassifications of land cover classes.

Eight regions, numbered 1-8 in Fig. 7(d) were selected for detailed zooming and comparative analysis to facilitate the comparison of classification results among the four experiments.

The zoomed regions, as shown in Fig. 8, encompass all 12 land cover classes. Fig. 8 displays the sentinel original image in the first column, while the 2nd to 5th columns presents the results of Experiments 1 to 4. In Experiment 1, the comparative analysis reveals that the red areas of oils within the red circle are smaller. The pixel-based method used in Experiment 1 results in the misclassification of oil wells as green reeds and orange roads. This is due to the method's lack of reliance on region connectivity and consistency, which may lead to misjudgment of the land cover classes. Areas 5 to 8 of Experiment 1 demonstrated the intensified pepper-salt phenomenon in the red circular area. Conversely, the other three experiments, based on the object-oriented method, exhibit superior overall classification results.

In Experiment 2, firstly, in the fourth area, the canals and ditches class are misclassified as oil wells. Secondly, in the fifth area, the restoration area is misclassified as buildings. Thirdly, in the second area, the canals and ditches are misclassified as aquaculture in the red circular area, taking into account the time series perspective. Lastly, in the sixth area, the restoration area is misclassified as Suaeda salsa, roads, and canal, ditch. The varying water levels of canals and ditches in different seasons, coupled with the absence of temporal information, may cause the algorithm to mistakenly classify them as oil wells. The similarity in appearance between buildings and degraded intertidal zones in different seasons can also lead to misclassification due to the algorithm's inability to accurately capture their distinctive characteristics. Additionally, in certain areas, the spectral properties of the restoration are can resemble those of Suaeda salsa, roads, and canals, resulting in misclassifications due to the lack of temporal variation for differentiation.

The comparative analysis of Experiment 3 reveals that in the second area, oil wells are misclassified as roads, while in the third area, the canals and ditches are misclassified as aquaculture. All features likely possess overlapping characteristics
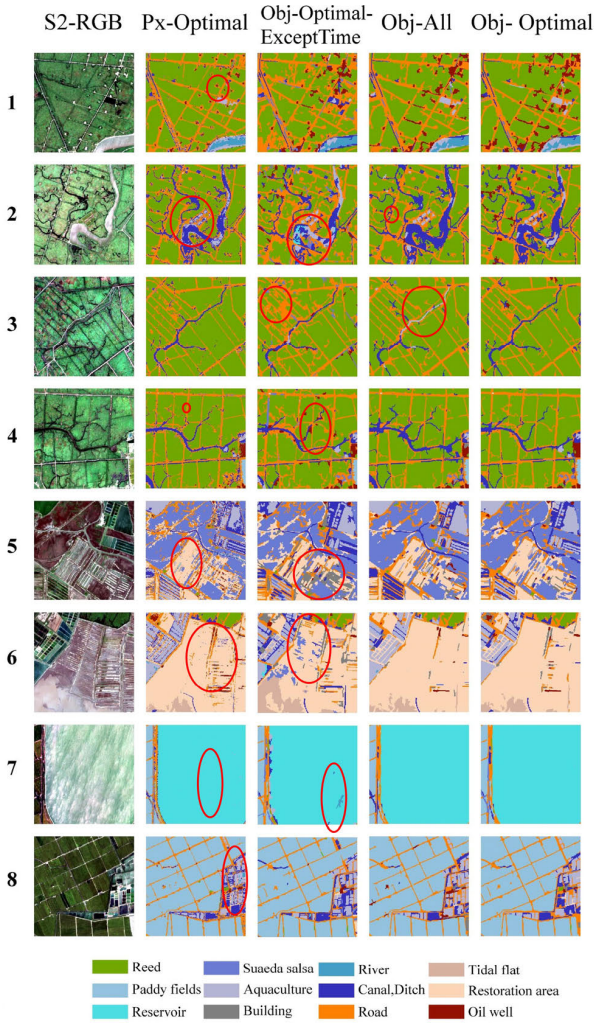
FIGURE 8. Detailed classification result map.

FIGURE 9. Confusion matrices of the four experiments.

that disrupt the algorithm and lead to the misclassification of oil wells and canals. In conclusion, the object-oriented method greatly enhances the overall classification results and successfully mitigates pixel-level misclassifications and spectral confusion.

Moreover, the inclusion of temporal information diminishes the pepper-salt phenomenon and enhances the accuracy of land cover classes across various seasons and temporal changes. These findings establish that the wetland classification method, which combines object-oriented and time series approaches, improve classification performance and accuracy in classification results, particularly when handling seasonal variations in land cover and the pepper-salt phenomenon.

2) QUANTITATIVE EVALUATION RESULTS OF ACCURACY

This article presents a quantitative evaluation of classification methods for four experiments. The evaluation includes the use of a confusion matrix (Fig. 9), as well as metrics such as producer accuracy, user accuracy, and overall accuracy (Table 4). From the results presented in Table 4, it is evident that the proposed Obj-Optimal classification method
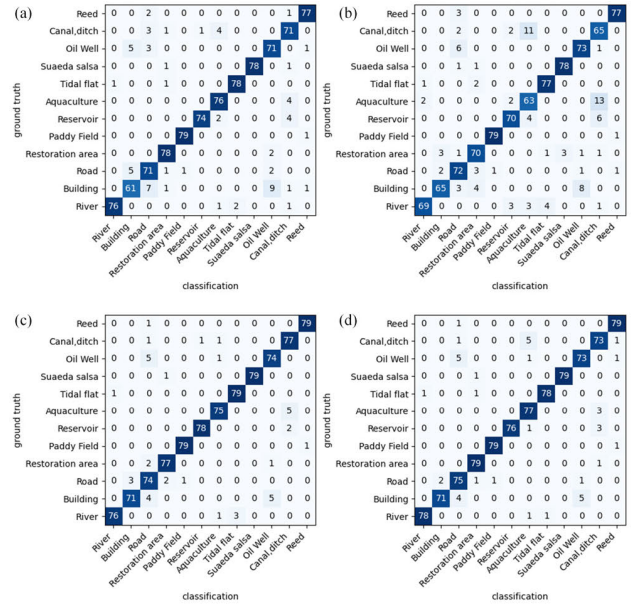
(Experiment 4) achieves an overall accuracy of 95.52% and a Kappa coefficient of 0.95. Except for the building category, the producer accuracy for the other eleven land use/land cover types is above 90%, and the user accuracy for all categories, except roads, is also above 90%. However, the producer accuracy for the building category remains the highest among all four experiments at 88.75%. Additionally, roads have the highest user accuracy among the four experiments at 87.21%.

Using the training set described in Section II, part B, and the original 9 spectral bands as features in Section III, part B, we compared the classification accuracy for the Liaohe Estuary wetland using three machine learning methods: SVM, RF, and deep learning SegUnet++. The type of SVM is set to C-Support Vector Classification (C-SVC), with the kernel type being Radial Basis Function (RBF). The gamma value is set to 1, and the cost parameter is 10. The parameters of RF are set to 110. The SegUnet++ method is implemented based on the deep learning module of ENVI 5.7 version. The initial model patch size was set to 464, and random parameter training tools are utilized. The iteration is set to 32 times. The results with better classification performance are selected for accuracy verification, retaining the overall optimal classification results. The accuracies obtained by these methods were 81.46, 89.38, and 79.17, respectively. The corresponding Kappa coefficients were 0.80, 0.88, and 0.77, respectively. Among the classification methods, RF achieved the highest overall accuracy. Details of user accuracy and producer accuracy for each land cover type under the three methods can be found in columns 1-6 of Table 4. It is worth noting that the classification accuracies obtained by the three methods are lower than those of the latter four experiments.

Upon comparative analysis of the four experiments conducted in this article, it is evident that the Obj-Optimal method proposed in Experiment 4 outperforms the

TABLE 4. Accuracy of the traditional methods and accuracy of experiment 1 to 4.

(%)	SegUnet++		SVM		RF		Px-Optimal		Obj-Optimal-ExceptTime		Obj-All		Obj-Optimal	
	PA	UA	PA	UA	PA	UA	PA	UA	PA	UA	PA	UA	PA	UA
River	83.75	98.53	83.75	87.01	91.25	91.25	95	98.7	86.25	95.83	95.00	98.70	97.50	98.73
Building	90	97.3	76.25	72.62	75.00	71.43	76.25	85.92	81.25	92.86	88.75	95.95	88.75	97.26
Road	81.25	44.52	78.75	86.30	82.50	89.19	88.75	82.56	90.00	81.82	92.50	85.06	93.75	87.21
Restoration Area	87.5	100	83.75	81.71	82.50	82.50	97.5	93.98	87.50	87.50	96.25	96.25	98.75	96.34
Paddy Field	86.25	100	98.75	98.75	98.75	100	98.75	98.75	98.75	98.75	98.75	98.75	98.75	98.75
Reservoir	100	76.19	100	67.23	100	98.77	92.5	98.67	87.50	90.91	97.50	98.73	95.00	100
Aquaculture	82.5	59.46	56.25	59.21	85.00	89.47	95	91.57	78.75	77.78	93.75	96.15	96.25	90.59
Tidal flat	98.75	91.86	91.25	87.95	95.00	92.68	97.5	97.5	96.25	93.90	98.75	96.34	97.50	98.73
Suaeda salsa	100	83.33	100	87.91	100	94.12	97.5	100	97.50	96.30	98.75	100	98.75	100
Oil Well	87.5	87.5	76.25	81.33	78.75	81.82	88.75	84.52	91.25	87.95	92.50	92.50	91.25	92.41
Canal, ditch	23.75	86.36	33.75	79.41	86.25	87.34	88.75	85.54	81.25	74.71	96.25	91.67	91.25	91.25
Reed	28.75	100	98.75	91.86	97.50	93.98	96.25	96.25	96.25	97.47	98.75	98.75	98.75	96.34
OA	79.17%		81.46%		89.38%		92.71%		89.38%		95.63%		95.52%	
Kappa	0.77		0.80		0.88		0.92		0.88		0.95		0.95	

Px-Optimal method in Experiment 1, resulting in a 2.81% increase in overall accuracy and a 0.03% increase in the Kappa coefficient. Regarding user accuracy, apart from the aquaculture category, accuracies in other categories have shown varying degrees of improvement. The most notable enhancement was observed in the building category, with a significant 11.34% increase in user accuracy. The accuracy for natural wetlands (tidal flats, Suaeda salsa, reeds, and rivers) increased by an average of 0.34%, while artificial wetlands (restoration areas, reservoirs, and canals) saw an average increase of 2.35%. Furthermore, non-wetland areas (buildings, roads, and oil wells) experienced an average accuracy improvement of 7.96%. Contrarily, user accuracy in the aquaculture category declined. Upon review of the confusion matrix, displayed in Figs. 9(a) and 9(d), this decrease can be attributed to misclassifications of oil wells and canals as aquaculture areas during the classification process. This misclassification arose from canals being segmented into objects resembling aquaculture areas in size, leading to ambiguous shape features and subsequent errors. Additionally, the producer accuracies for the 12 land cover categories exhibited varying enhancements, with the building category showing the highest increase at 12.5%. Upon category analysis, the accuracy for natural wetlands (rivers, tidal flat, Suaeda salsa, reeds) increased on average by 1.56%, while artificial wetlands (restoration area, reservoir, aquaculture, canals, paddy fields) saw an average increase of 1.5%.

Non-wetland areas (buildings, roads, oil wells) also experienced an average accuracy improvement of 6.67%. Overall, the analysis of Experiment 1 and Experiment 4 suggests that object-oriented methods generally outperform pixel-based classification methods.

The results of the comparative analysis demonstrate that Experiment 4, utilizing the Obj-Optimal-ExceptTime method, exhibited a 6.14% increase in overall accuracy and a 0.07 improvement in the Kappa coefficient, as compared to Experiment 2. In terms of user accuracy, Experiment 4 with the Obj-Optimal method outperformed Experiment 2 with the Obj-Optimal-ExceptTime method, except for the reed category. However, Experiment 4 misclassified certain land cover types - oil wells, canals, ditches, and paddy fields - as reeds, potentially due to noise or outliers in the temporal data, which could disrupt the accuracy of the classification algorithm. Moreover, the proximity of these land cover types to reed fields presents an additional challenge in their classification. Notably, natural wetlands (including rivers, paddy fields, tidal flat, and Suaeda salsa) experienced an average improvement of 2.86% in user accuracy, artificial wetlands (retired tidal flat, reservoirs, aquaculture, and canals, ditches) saw an average improvement of 11.56%, while non-wetlands (buildings, roads, oil wells) demonstrated an average improvement of 4.75%. The analysis of producer accuracy indicated a significant improvement across all land categories, with an average improvement of 6.15%. Particularly, the aquaculture category

displayed the highest increase of 17.5%. In terms of producer accuracy, natural wetlands improved on average by 3.25%, artificial wetlands by 11.56%, and non-wetlands by 3.75%. Taken together, the findings from Experiment 2 and Experiment 4 highlight the utility of optimal temporal features in minimizing misclassifications and enhancing accuracy in land cover classification.

Experiment 4 with the Obj-Optimal method exhibited a slightly lower overall accuracy compared to Experiment 3 with the Obj-All method, with a difference of 0.11%. However, the Kappa coefficient remained the same. Concerning user accuracy, natural wetlands (including rivers, paddy fields, tidal flat, and Suaeda salsa) showed an average improvement of 0.61%, artificial wetlands (restoration area and reservoirs) had an average improvement of 0.68%, and non-wetlands (buildings and roads) demonstrated an average improvement of 1.73%. Nevertheless, the accuracy of aquaculture, oil wells, canals, ditches, and reeds declined by 5.57, 0.09, 0.42, and 2.41 percentage points, respectively. The decrease in aquaculture accuracy can be attributed to increased misclassifications between canals, and reservoirs. The decrease in oil well accuracy was due to fewer pixels being correctly predicted. The decrease in canals and ditches accuracy resulted from an increase in misclassifications between restoration area and canals, ditches, as well as a lower number of pixels being correctly predicted. The decline in reed accuracy was a consequence of increased misclassifications between oil wells, canals, ditches, and reeds. Regarding producer accuracy, the first-level classification revealed an average improvement of 0.83% for artificial wetlands (rivers, paddy fields, Suaeda salsa, reeds), 2.5% for artificial wetlands (restoration area, aquaculture), and 0.63% for non-wetlands (buildings, roads). However, the producer accuracy of reservoirs, tidal flats, oil wells, and canals was slightly lower, particularly for canals and ditches, which had a 5% decrease in producer accuracy. This decrease primarily resulted from increased misclassifications between canals, ditches, and aquaculture due to disparities in texture features. Experiment 4 included only one type of texture feature, resulting in decreased accuracy in canals and ditches extraction. From Figs. 9(c) and 9(d), it is evident that the decrease in producer accuracy for reservoirs was due to increased misclassifications with aquaculture, for tidal flat it resulted from increased misclassifications with restoration area, and for oil wells, it was because of increased misclassifications with reeds. Overall, Experiment 4 and Experiment 3 yielded similar results in the classification of the 12 land categories, effectively extracting all land categories. This indicates that the selected features objectively captured the distinctions among different land categories and possessed the ability to extract diverse land use/cover types in the study area. In terms of time efficiency, Experiment 4 took an average of 1753 milliseconds for 10 runs, while Experiment 3 required an average of 5703 milliseconds for 10 runs. Accordingly, Experiment 4 demonstrated a time efficiency 3.25 times higher than that of Experiment 3, highlighting its superior performance.

Fig. 10. depicts the proportional distribution of the 12 land cover types within the study area. Experiments 1, 2, and 4 manifest a strong degree of consistency in their outcomes. Conversely, Experiment 2 yields underestimated values for the river and restoration area categories, resulting in discrepancies in the overall proportions when compared to the other three methods.
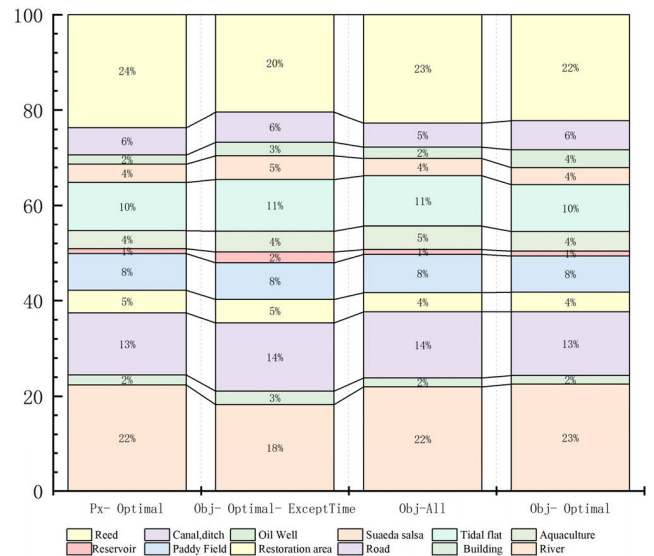

FIGURE 10. The proportions of land cover areas from the four experiments to the total area.

To summarize, Experiment 4 combines object-based and time-series techniques for wetland classification. This integration effectively mitigates pixel-based misclassifications and spectral ambiguity. Through the incorporation of optimal temporal features, Experiment 4 successfully reduces misclassifications, enhances overall accuracy, and diminishes computational demands.

V. DISCUSSION

This study employed multiple remote sensing image processing methods, namely SNIC, GLCM, and RF, available on the GEE platform, for extracting the spatial distribution of 12 land cover types within the Liaohe Estuary Wetland Nature Reserve utilizing Sentinel-2 satellite imagery. Firstly, the algorithm employed in this study attained superior accuracy and reduced fragmentation in contrast to pixel-based methods by integrating spectral, standard deviation, shape, and texture features of the land cover types. Secondly, this study further enhanced the classification accuracy by incorporating the characteristic temporal features of each object. To optimize the method's efficiency without compromising accuracy, the selection process prioritized the most significant features from an extensive array. During the process of selecting optimal features, this study accounted for feature categorization to mitigate concerns like disparate measurement units and the omission of crucial features. The suggested integration of

object-oriented and temporal features provides the following benefits:

A. ADVANTAGES OF OBJECT-ORIENTED APPROACH

In this study, we employed an image segmentation algorithm to partition the multi-temporal images into distinct "blocks". Each pixel within a "block" was assigned to the same class, effectively mitigating the detrimental effects of speckle noise on classification accuracy. The research findings indicate that the integration of the object-oriented classification method with time series Sentinel-2 data can lead to a substantial improvement in the classification accuracy of the wetland study area, surpassing a high threshold (OA > 95%). Similarly to numerous other studies, the pixel-based classification method is susceptible to "noise", leading to fragmented classification outcomes. Neglecting neighboring pixels often gives rise to the occurrence of "salt and pepper" artifacts. Therefore, object-oriented classification outperforms pixel-based classification, delivering superior results [56], [57].

B. ADVANTAGES OF TEMPORAL FEATURES

The study results demonstrate that time series of wetness and greenness components obtained through Tasseled Cap Trasform can offer insights into the temporal dynamics of land cover, facilitating enhanced discrimination of evolving land cover categories in wetland classification and leading to improved classification accuracy. Moreover, existing literature supports the notion that incorporating multi-seasonal factors proves highly effective in capturing wetland land cover changes over time. Specifically targeted land cover categories with high spectral similarity include rivers, reservoirs, aquaculture, and canals. The producer's accuracies improved by 11.25%, 7.5%, 17.5%, and 10%, respectively, while the user's accuracies improved by 2.9%, 9.09%, 12.81%, and 16.54%, respectively. For instance, Deventer et al. conducted a study on the significance of multi-seasonal imagery in distinguishing wetland and upland regions, revealing that the incorporation of imagery from all four seasons yielded the highest overall accuracy [58]. Wang et al. successfully integrated the temporal dimension into a hierarchical decision tree framework, enabling effective differentiation between coastal aquaculture ponds and other water bodies. The timing of data collection significantly impacts the quality of outcomes [18]. By effectively capturing the variations in wetness and greenness specific to each land cover type, optimal time series data substantially enhance the accuracy of information extraction.

C. ADVANTAGES OF FEATURE SELECTION

The classification performance between Experiment 4 and Experiment 3 shows minimal variation, as observed through visual interpretation, quantitative evaluation, and area comparison. Following the reduction of feature dimensions, the JM distance of the 12 land cover types surpasses 1.9, signifying the strong discriminative ability of the selected features

for each land cover type. Furthermore, both the overall accuracy and Kappa coefficient exhibit minimal variation, indicating the excellent land cover extraction capability of our method, which is also 3.25 times more time-efficient when compared to the full feature method, resulting in a considerable time advantage.

D. LIMITATIONS AND FUTURE RESEARCH DIRECTIONS

The proposed method in this paper has yielded promising results; however, there remain a few issues that need to be addressed. Firstly, the temporal dimension may be overlooked due to the non-uniform coverage of time series data caused by cloud cover and satellite orbit. To further exploit time series data, an important future research direction is to address the challenge of cloud filling in remote sensing images. Secondly, the determination of the optimal segmentation scale lacks an automatic and efficient method. In this paper, the optimal segmentation scale was selected through repetitive experiments and visual judgment, which may introduce certain errors. Different land cover types require different segmentation scales. In this study, a segmentation parameter of 10 was chosen. However, for small water bodies and buildings, this segmentation scale may be too large, and this should be explored in future research. Additionally, building upon this foundation, the proposed research method can be extended to extract wetland land cover types across multiple years and conduct corresponding change detection.

VI. CONCLUSION

In this study, we utilized multi-temporal Sentinel-2 images on the Google Earth Engine (GEE) platform to extract land use/cover information in the Liaohe Estuary area. The SNIC algorithm and random forest algorithm were employed, along with texture, spectral, and geometric features. The results demonstrated satisfactory extraction accuracy and precision. The specific comparative conclusions are as follows:

The object-based approach exhibited exceptional performance in the wetland study area by mitigating the "salt and pepper" effect and enhancing classification accuracy. Unlike the pixel-based approach, the object-based technique focuses on objects and encompasses the integration of spectral, geometric, and texture information to exploit the correlations among neighboring pixels, the classification accuracy and Kappa coefficient exhibited an increase of 2.81% and 0.03, respectively.

When combining the object-based approach with selected features in this study, the overall classification accuracy and Kappa coefficient experienced enhancements of 6.14% and 0.07, respectively, compared to the object-based approach without the inclusion of temporal features. This demonstrates that the selected combinations of temporal features significantly augment information extraction accuracy.

By combining random forest (RF) and extremely randomized trees (ERT) in this study, land features were effectively

differentiated using time and shape features chosen based on their contributions. This approach concurrently reduces data redundancy, enhances computational efficiency, and aligns with the requirements for wetland extraction in the study area.

REFERENCES

[1] C. Xie, J. Xu, Y. Shao, B. Cui, K. Goel, Y. Zhang, and M. Yuan, "Long term detection of water depth changes of coastal wetlands in the Yellow River Delta based on distributed scatterer interferometry," *Remote Sens. Environ.*, vol. 164, pp. 238–253, Jul. 2015, doi: 10.1016/j.rse.2015.04.010.

[2] A. Jamali and M. Mahdianpari, "Swin Transformer for complex coastal wetland classification using the integration of Sentinel-1 and Sentinel-2 imagery," *Water*, vol. 14, no. 2, p. 178, Jan. 2022, doi: 10.3390/w14020178.

[3] A. LaRocque, C. Phiri, B. Leblon, F. Pirotti, K. Connor, and A. Hanson, "Wetland mapping with Landsat 8 OLI, Sentinel-1, ALOS-1 PALSAR, and LiDAR data in Southern New Brunswick, Canada," *Remote Sens.*, vol. 12, no. 13, p. 2095, 2020, doi: 10.3390/rs12132095.

[4] Y. Liu, Z. Guo, P. Zhang, J. Du, P. Gao, and Z. Zhang, "Diversity and structure of vegetation rhizosphere bacterial community in various habitats of Liaohekou Coastal Wetlands," *Sustainability*, vol. 14, no. 24, p. 16396, Dec. 2022, doi: 10.3390/su142416396.

[5] X. Li, C. J. Anderson, Y. Wang, and G. Lei, "Waterbird diversity and abundance in response to variations in climate in the Liaohe Estuary, China," *Ecological Indicators*, vol. 132, Dec. 2021, Art. no. 108286, doi: 10.1016/j.ecolind.2021.108286.

[6] K. Chen, P. Cong, L. Qu, S. Liang, and Z. Sun, "Annual variation of the landscape pattern in the Liao River Delta wetland from 1976 to 2020," *Ocean Coastal Manage.*, vol. 224, Jun. 2022, Art. no. 106175, doi: 10.1016/j.ocecoaman.2022.106175.

[7] Z. Zhu, S. Qiu, and S. Ye, "Remote sensing of land change: A multifaceted perspective," *Remote Sens. Environ.*, vol. 282, Dec. 2022, Art. no. 113266, doi: 10.1016/j.rse.2022.113266.

[8] Y. Wang, S. Jin, and G. Dardanelli, "Vegetation classification and evaluation of Yancheng Coastal Wetlands based on random forest algorithm from Sentinel-2 images," *Remote Sens.*, vol. 16, no. 7, p. 1124, Mar. 2024, doi: 10.3390/rs16071124.

[9] I. Ivanova, T. Spasova, and N. Stankova, "Using Sentinel-2 data for efficient monitoring and modeling of wetland protected areas," in *Proc. 9th Int. Conf. Remote Sens. Geoinformation Environ. (RSCy)*, Sep. 2023, pp. 658–665, doi: 10.1117/12.2681790.

[10] A.-L. Balogun, S. T. Yekeen, B. Pradhan, and O. F. Althuwaynee, "Spatio-temporal analysis of oil spill impact and recovery pattern of coastal vegetation and wetland using multispectral satellite Landsat 8-OLI imagery and machine learning models," *Remote Sens.*, vol. 12, no. 7, p. 1225, Apr. 2020, doi: 10.3390/rs12071225.

[11] B. Fu, P. Zuo, M. Liu, G. Lan, H. He, Z. Lao, Y. Zhang, D. Fan, and E. Gao, "Classifying vegetation communities Karst wetland synergistic use of image fusion and object-based machine learning algorithm with Jilin-1 and UAV multispectral images," *Ecological Indicators*, vol. 140, Jul. 2022, Art. no. 108989, doi: 10.1016/j.ecolind.2022.108989.

[12] R. M. Prentice, M. V. Peciña, R. D. Ward, T. F. Bergamo, C. B. Joyce, and K. Sepp, "Machine learning classification and accuracy assessment from high-resolution images of coastal wetlands," *Remote Sens.*, vol. 13, no. 18, p. 3669, Sep. 2021, doi: 10.3390/rs13183669.

[13] C. Xu, J. Wang, Y. Sang, K. Li, J. Liu, and G. Yang, "An effective deep learning model for monitoring mangroves: A case study of the Indus Delta," *Remote Sens.*, vol. 15, no. 9, p. 2220, Apr. 2023, doi: 10.3390/rs15092220.

[14] A. Abdollahi, B. Pradhan, and A. M. Alamri, "An ensemble architecture of deep convolutional Segnet and Unet networks for building semantic segmentation from high-resolution aerial images," *Geocarto Int.*, vol. 37, no. 12, pp. 3355–3370, Jun. 2022, doi: 10.1080/10106049.2020.1856199.

[15] C. J. Anderson, D. Heins, K. C. Pelletier, and J. F. Knight, "Improving machine learning classifications of phragmites Australis using object-based image analysis," *Remote Sens.*, vol. 15, no. 4, p. 989, Feb. 2023, doi: 10.3390/rs15040989.

[16] M. Wang, D. Mao, Y. Wang, X. Xiao, H. Xiang, K. Feng, L. Luo, M. Jia, K. Song, and Z. Wang, "Wetland mapping in East Asia by two-stage object-based random forest and hierarchical decision tree algorithms on Sentinel-1/2 images," *Remote Sens. Environ.*, vol. 297, Nov. 2023, Art. no. 113793, doi: 10.1016/j.rse.2023.113793.

[17] M. Zhang and H. Lin, "Wetland classification using parcel-level ensemble algorithm based on Gaofen-6 multispectral imagery and Sentinel-1 dataset," *J. Hydrol.*, vol. 606, Mar. 2022, Art. no. 127462, doi: 10.1016/j.jhydrol.2022.127462.

[18] M. Wang, D. Mao, X. Xiao, K. Song, M. Jia, C. Ren, and Z. Wang, "Interannual changes of coastal aquaculture ponds in China at 10-m spatial resolution during 2016–2021," *Remote Sens. Environ.*, vol. 284, Jan. 2023, Art. no. 113347, doi: 10.1016/j.rse.2022.113347.

[19] P. Xu, Z. Niu, and P. Tang, "Comparison and assessment of NDVI time series for seasonal wetland classification," *Int. J. Digit. Earth*, vol. 11, no. 11, pp. 1103–1131, Nov. 2018, doi: 10.1080/17538947.2017.1375563.

[20] X. Yan, Z. Niu, Y. Li, Q. Han, and H. Zhang, "Reliability evaluation of wetland samples based on historical thematic maps," in *Proc. IEEE Int. Geosci. Remote Sens. Symp.*, Sep. 2020, pp. 4754–4757, doi: 10.1109/IGARSS39084.2020.9324288.

[21] Y. Chen, Z. Niu, S. Hu, and H. Zhang, "Dynamic monitoring of Dongting Lake wetland using time-series MODIS imagery," *J. Hydraulic Eng.*, vol. 47, no. 9, pp. 1093–1104, 2016, doi: 10.13243/j.cnki.slxb.20151245.

[22] B. Dunn, E. Ai, M. J. Alger, B. Fanson, K. C. Fickas, C. E. Krause, L. Lymburner, R. Nanson, P. Papas, M. Ronan, and R. F. Thomas, "Wetlands insight tool: Characterising the surface water and vegetation cover dynamics of individual wetlands using multidecadal Landsat satellite data," *Wetlands*, vol. 43, no. 4, p. 37, Apr. 2023.

[23] *Ramsar Sites Information Service (2022) Ramsar*. Accessed: Sep. 16, 2022. [Online]. Available: https://rsis.ramsar.org/ris/1441

[24] J. Xing and D. Meng, "Wetland monitoring application in panjin city based on remote sensing data of wide-band imaging spectrometer of Tiangong-2," in *Proc. Tiangong-2 Remote Sens. Appl. Conf., Technol., Method Appl.*, 2019, pp. 300–311.

[25] X. Yan, M. Liu, J. Zhong, J. Guo, and W. Wu, "How human activities affect heavy metal contamination of soil and sediment in a long-term reclaimed area of the Liaohe River Delta, North China," *Sustainability*, vol. 10, no. 2, p. 338, Jan. 2018, doi: 10.3390/su10020338.

[26] N. Gorelick, M. Hancher, M. Dixon, S. Ilyushchenko, D. Thau, and R. Moore, "Google Earth Engine: Planetary-scale geospatial analysis for everyone," *Remote Sens. Environ.*, vol. 202, pp. 18–27, Dec. 2017, doi: 10.1016/j.rse.2017.06.031.

[27] R. Achanta and S. Süsstrunk, "Superpixels and polygons using simple non-iterative clustering," in *Proc. IEEE Conf. Comput. Vis. Pattern Recognit. (CVPR)*, Jul. 2017, pp. 4895–4904, doi: 10.1109/CVPR.2017.520.

[28] M. Mahdianpari, B. Salehi, F. Mohammadimanesh, S. Homayouni, and E. Gill, "The first wetland inventory map of Newfoundland at a spatial resolution of 10 m using Sentinel-1 and Sentinel-2 data on the Google Earth Engine cloud computing platform," *Remote Sens.*, vol. 11, no. 1, p. 43, Dec. 2018, doi: 10.3390/rs11010043.

[29] R. Nedkov, "Orthogonal transformation of segmented images from the satellite Sentinel-2," *Comp. Rendus de l'Academie Bulgare des Sci.*, vol. 70, no. 5, pp. 687–692, 2017.

[30] K. Luo and F. Tao, "Method for wetland type extraction using remote sensing combing object-oriented and tasseled cap transformation," *Trans. Chin. Soc. Agricult. Eng.*, vol. 33, no. 3, pp. 198–203, 2017, doi: 10.11975/j.issn.1002-6819.2017.03.027.

[31] T. Blaschke, G. J. Hay, M. Kelly, S. Lang, P. Hofmann, E. Addink, R. Q. Feitosa, F. Van der Meer, H. van der Werff, F. van Coillie, and D. Tiede, "Geographic object-based image analysis-towards a new paradigm," *ISPRS J. Photogramm. remote Sens.*, vol. 87, pp. 180–191, Jan. 2014, doi: 0.1016/j.isprsjprs.2013.09.014.

[32] M. Kim, T. A. Warner, M. Madden, and D. S. Atkinson, "Multi-scale GEO-BIA with very high spatial resolution digital aerial imagery: Scale, texture and image objects," *Int. J. Remote Sens.*, vol. 32, no. 10, pp. 2825–2850, May 2011, doi: 10.1080/01431161003745608.

[33] M. Kim, M. Madden, and B. Xu, "GEOBIA vegetation mapping in great smoky mountains national park with spectral and non-spectral ancillary information," *Photogrammetric Eng. Remote Sens.*, vol. 76, no. 2, pp. 137–149, Feb. 2010, doi: 10.14358/pers.76.2.137.

[34] T. Warner, "Kernel-based texture in remote sensing image classification," *Geography Compass*, vol. 5, no. 10, pp. 781–798, Oct. 2011, doi: 10.1111/j.1749-8198.2011.00451.x.

[35] R. M. Haralick, K. Shanmugam, and I. Dinstein, "Textural features for image classification," *IEEE Trans. Syst., Man, Cybern.*, vol. SMC-3, no. 6, pp. 610–621, Nov. 1973, doi: 10.1109/TSMC.1973.4309314.

[36] R. W. Conners, M. M. Trivedi, and C. A. Harlow, "Segmentation of a high-resolution urban scene using texture operators," *Comput. Vis., Graph., Image Process.*, vol. 25, no. 3, pp. 273–310, Mar. 1984, doi: 10.1016/0734-189x(84)90197-x.

[37] N. Iqbal, R. Mumtaz, U. Shafi, and S. M. H. Zaidi, "Gray level co-occurrence matrix (GLCM) texture based crop classification using low altitude remote sensing platforms," *PeerJ Comput. Sci.*, vol. 7, p. e536, May 2021, doi: 10.7717/peerj-cs.536.

[38] A. Tassi and M. Vizzari, "Object-oriented LULC classification in Google Earth Engine combining SNIC, GLCM, and machine learning algorithms," *Remote Sens.*, vol. 12, no. 22, p. 3776, Nov. 2020, doi: 10.3390/rs12223776.

[39] M. Karlson, H. Reese, and M. Ostwald, "Tree crown mapping in managed woodlands (Parklands) of semi-arid west Africa using WorldView-2 imagery and geographic object based image analysis," *Sensors*, vol. 14, no. 12, pp. 22643–22669, Nov. 2014, doi: 10.3390/s141222643.

[40] M. Kucharczyk, G. J. Hay, S. Ghaffarian, and C. H. Hugenholtz, "Geographic object-based image analysis: A primer and future directions," *Remote Sens.*, vol. 12, no. 12, p. 2012, Jun. 2020, doi: 10.3390/rs12122012.

[41] P. Geurts, D. Ernst, and L. Wehenkel, "Extremely randomized trees," *Mach. Learn.*, vol. 63, no. 1, pp. 3–42, Apr. 2006.

[42] J. Simm, I. Magrans De Abril, and M. Sugiyama, "Tree-based ensemble multi-task learning method for classification and regression," *IEICE Trans. Inf. Syst.*, vol. 97, no. 6, pp. 1677–1681, 2014, doi: 10.1587/transinf.e97.d.1677.

[43] D. Thakur and S. Biswas, "Guided regularized random forest feature selection for smartphone based human activity recognition," *J. Ambient Intell. Humanized Comput.*, vol. 14, no. 7, pp. 9767–9779, Jul. 2023.

[44] X. Wang, L. Tan, and J. Fan, "Performance evaluation of mangrove species classification based on multi-source remote sensing data using extremely randomized trees in Fucheng town, Leizhou city, Guangdong province," *Remote Sens.*, vol. 15, no. 5, p. 1386, Mar. 2023, doi: 10.3390/rs15051386.

[45] T. Nery, R. Sadler, M. Solis-Aulestia, B. White, M. Polyakov, and M. Chalak, "Comparing supervised algorithms in land use and land cover classification of a Landsat time-series," in *Proc. IEEE Int. Geosci. Remote Sens. Symp. (IGARSS)*, Jul. 2016, pp. 5165–5168, doi: 10.1109/IGARSS.2016.7730346.

[46] G. M. Foody, "Status of land cover classification accuracy assessment," *Remote Sens. Environ.*, vol. 80, no. 1, pp. 185–201, Apr. 2002, doi: 10.1016/s0034-4257(01)00295-4.

[47] A. Jamali, M. Mahdianpari, B. Brisco, J. Granger, F. Mohammadimanesh, and B. Salehi, "Deep forest classifier for wetland mapping using the combination of Sentinel-1 and Sentinel-2 data," *GIScience Remote Sens.*, vol. 58, no. 7, pp. 1072–1089, Oct. 2021, doi: 10.1080/15481603.2021.1965399.

[48] J. E. Granger, M. Mahdianpari, T. Puestow, S. Warren, F. Mohammadimanesh, B. Salehi, and B. Brisco, "Object-based random forest wetland mapping in Conne River, Newfoundland, Canada," *J. Appl. Remote Sens.*, vol. 15, no. 3, Aug. 2021, Art. no. 038506, doi: 10.1117/1.jrs.15.038506.

[49] M. Mahdianpari, B. Salehi, F. Mohammadimanesh, and M. Motagh, "Random forest wetland classification using ALOS-2 L-band, RADARSAT-2 C-band, and TerraSAR-X imagery," *ISPRS J. Photogramm. Remote Sens.*, vol. 130, pp. 13–31, Aug. 2017, doi: 10.1016/j.isprsjprs.2017.05.010.

[50] P. O. Gislason, J. A. Benediktsson, and J. R. Sveinsson, "Random forests for land cover classification," *Pattern Recognit. Lett.*, vol. 27, no. 4, pp. 294–300, Mar. 2006, doi: 10.1016/j.patrec.2005.08.011.

[51] Y. Jin, X. Liu, Y. Chen, and X. Liang, "Land-cover mapping using random forest classification and incorporating NDVI time-series and texture: A case study of Central Shandong," *Int. J. Remote Sens.*, vol. 39, no. 23, pp. 8703–8723, Dec. 2018, doi: 10.1080/01431161.2018.1490976.

[52] R. G. Congalton, "A review of assessing the accuracy of classifications of remotely sensed data," *Remote Sens. Environ.*, vol. 37, no. 1, pp. 35–46, Jul. 1991, doi: 10.1016/0034-4257(91)90048-b.

[53] R. G. Congalton and K. Green, *Assessing the Accuracy of Remotely Sensed Data: Principles and Practices*. Boca Raton, FL, USA: CRC Press, 2019.

[54] M. Dabboor, S. Howell, M. Shokr, and J. Yackel, "The Jeffries–Matusita distance for the case of complex Wishart distribution as a separability criterion for fully polarimetric SAR data," *Int. J. Remote Sens.*, vol. 35, no. 19, pp. 6859–6873, 2014, doi: 10.5555/2684857.2684859.

[55] M. Zhang, Y. Zeng, and Y. Zhu, "Wetland mapping of donting lake basin based on time-series MODIS data and object-oriented method," *Nat. Remote Sens. Bull.*, vol. 21, no. 3, pp. 479–492, 2017, doi: 10.11834/jrs.20176129.

[56] Z. Qi, A. G.-O. Yeh, X. Li, and Z. Lin, "A novel algorithm for land use and land cover classification using RADARSAT-2 polarimetric SAR data," *Remote Sens. Environ.*, vol. 118, pp. 21–39, Mar. 2012, doi: 10.1016/j.rse.2011.11.001.

[57] S. Skakun, N. Kussul, A. Yu. Shelestov, M. Lavreniuk, and O. Kussul, "Efficiency assessment of multitemporal C-band Radarsat-2 intensity and Landsat-8 surface reflectance satellite imagery for crop classification in Ukraine," *IEEE J. Sel. Topics Appl. Earth Observ. Remote Sens.*, vol. 9, no. 8, pp. 3712–3719, Aug. 2016, doi: 10.1109/JSTARS.2015.2454297.

[58] H. van Deventer, M. A. Cho, and O. Mutanga, "Multi-season RapidEye imagery improves the classification of wetland and dryland communities in a subtropical coastal region," *ISPRS J. Photogramm. Remote Sens.*, vol. 157, pp. 171–187, Nov. 2019, doi: 10.1016/j.isprsjprs.2019.09.007.

SIEN GUO was born in Chaoyang, Liaoning, China, in 1998. She received the B.S. degree in information and electrical engineering from Shenyang Agricultural University, Shenyang, China, where she is currently pursuing the M.S. degree in information and electronic engineering. Her research interest includes remote sensing land classification.
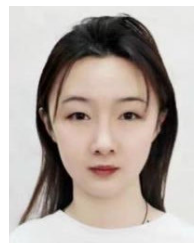
ZIYI FENG was born in Shenyang, China, in 1991. She received the B.S. and M.S. degrees from the School of Computer Science and Engineering, NEU, and the Ph.D. degree from the College of Water Conservancy, Shenyang Agricultural University, Shenyang, China, in 2022.

She is currently a Lecturer with the College of Information and Electrical Engineering, Shenyang Agricultural University. Her research interests include satellite remote sensing, remote sensing quantitative retrieval, image fusion, and image super-resolution.

PENG WANG is currently pursuing the M.S. degree with the College of Information and Electrical Engineering, Shenyang Agricultural University, Shenyang, China. His research interests include agricultural remote sensing and remote sensing image classification.
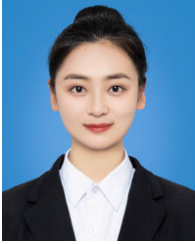
JIE CHANG received the B.S. degree in software engineering from Inner Mongolia University for Nationalities, Tongliao, China, in 2022. She is currently pursuing the M.S. degree in electronic information with Shenyang Agricultural University, Shenyang, China. Her research interests include remote sensing image data fusion and remote sensing land classification.

CHUNLING CHEN was born in Longyan, Fujian, China, in January 1971. She received the Ph.D. degree. She is currently a Professor with the School of Information and Electrical Engineering, Shenyang Agricultural University. Her research interests include agricultural electrification and informatization, and agricultural informatization.

HAO HAN was born in Shenyang, China, in 1997. He received the B.S. and M.S. degrees from the School of Geomatics, Liaoning Technical University, Fuxin, China. He is currently pursuing the Ph.D. degree with the College of Information and Electrical Engineering, Shenyang Agricultural University, Shenyang. His research interests include remote sensing, image processing, and computer vision.

HAIFU LI was born in Ledu, Qinghai, China, in January 1988. He received the master's degree, in 2013. He stayed in school to teach at the Water Conservancy College, Shenyang Agricultural University. He is mainly engaged in research on soil and water conservation and ecological environment assessment, with a focus on wetland water ecology.
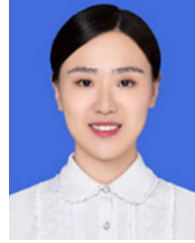
WEN DU received the B.S., M.S., and Ph.D. degrees from the College of Information and Electrical Engineering, Shenyang Agricultural University, Shenyang, China.

She is currently a Lecturer with the College of Information and Electrical Engineering, Shenyang Agricultural University. Her research interests include remote sensing and carbon neutrality.

● ● ●